Design optimization of ocean renewable energy converter using a combined Bi-level metaheuristic approach

Erfan Amini [a,1], Mahdieh Nasiri [b,1], Navid Salami Pargoo [a], Zahra Mozhgani [c], Danial Golbaz [d], Mehrdad Baniesmaeil [e], Meysam Majidi Nezhad [f], Mehdi Neshat [g,j], Davide Astiaso Garcia [h,*], Georgios Sylaios [i]

[a] Department of Civil, Environmental, and Ocean Engineering, Stevens Institute of Technology, Hoboken, NJ, United States
[b] Department Mechanical Engineering, Stevens Institute of Technology, Hoboken, NJ, United States
[c] Department of Civil and Environmental Engineering, Amirkabir University of Technology, Tehran, Iran
[d] Center for Applied Coastal Research, Civil and Environmental Engineering, University of Delaware, Newark, Delaware, United States
[e] Department of Marine Industries, Islamic Azad University, Science and Research Branch, Tehran, Iran
[f] Department of Sustainable Energy Systems, Mälardalen University, Västerås, SE 72123, Sweden
[g] Faculty of Engineering and Information Technology, University of Technology Sydney, Ultimo, NSW, Australia
[h] Department of Planning, Design, and Technology of Architecture, Sapienza University of Rome, Rome, Italy
[i] Laboratory of Ecological Engineering and Technology, Department of Environmental Engineering, Democritus University of Thrace, Xanthi, Greece
[j] Center for Artificial Intelligence Research and Optimisation, Torrens University Australia, Brisbane, QLD 4006, Australia

ARTICLE INFO

ABSTRACT

In recent years, there has been an increasing interest in renewable energies in view of the fact that fossil fuels are the leading cause of catastrophic environmental consequences. Ocean wave energy is a renewable energy source that is particularly prevalent in coastal areas. Since many countries have tremendous potential to extract this type of energy, a number of researchers have sought to determine certain effective factors on wave converters' performance, with a primary emphasis on ambient factors. In this study, we used metaheuristic optimization methods to investigate the effects of geometric factors on the performance of an Oscillating Surge Wave Energy Converter (OSWEC), in addition to the effects of hydrodynamic parameters. To do so, we used CATIA software to model different geometries which were then inserted into a numerical model developed in Flow3D software. A Ribed-surface design of the converter's flap is also introduced in this study to maximize wave-converter inter-action. Besides, a Bi-level Hill Climbing Multi-Verse Optimization (HCMVO) method was also developed for this application. The results showed that the converter performs better with greater wave heights, flap freeboard heights, and shorter wave periods. Additionally, the added ribs led to more wave-converter interaction and better performance, while the distance between the flap and flume bed negatively impacted the performance. Finally, tracking the changes in the five-dimensional objective function revealed the optimum value for each parameter in all scenarios. This is achieved by the newly developed optimization algorithm, which is much faster than other existing cutting-edge metaheuristic approaches.

1. Introduction

The increase in energy demand, the limitations of fossil fuels, as well as environmental crises, such as air pollution and global warming, are the leading causes of calling more attention to harvesting renewable energy recently [1,2,3]. While still in its infancy, ocean wave energy has neither reached commercial maturity nor technological convergence. In recent decades, remarkable progress has been made in the marine energy domain, which is still in the early stage of development, to improve the technology performance level (TPL) [4,5] and technology readiness level (TRL) of wave energy converters (WECs). This has been achieved using novel modeling techniques [6,7,8,9,10,11,12,13,14] to gain the following advantages [15]: (i) As a source of sustainable energy, it contributes to the mix of energy resources that leads to greater diversity

and attractiveness for coastal cities and suppliers. [16] (ii) Since wave energy can be exploited offshore and does not require any land, in-land site selection would be less expensive and undesirable visual effects would be reduced. [17] (iii) When the best layout and location of offshore site are taken into account, permanent generation of energy will be feasible (as opposed to using solar energy, for example, which is time-dependent) [18].

In general, the energy conversion process can be divided into three stages in a WEC device, including primary, secondary, and tertiary stages [19,20]. In the first stage of energy conversion, which is the subject of this study, the wave power is converted to mechanical power by wave-structure interaction (WSI) between ocean waves and structures. Moreover, the mechanical power is transferred into electricity in the second stage, in which mechanical structures are coupled with power take-off systems (PTO). At this stage, optimal control strategies are useful to tune the system dynamics to maximize power output [10,13,12]. Furthermore, the tertiary energy conversion stage revolves around transferring the non-standard AC power into direct current (DC) power for energy storage or standard AC power for grid integration [21,22]. We discuss only the first stage regardless of the secondary and tertiary stages. While Page 1 of 16 WECs include several categories and technologies such as terminators, point absorbers, and attenuators [15,23], we focus on oscillating surge wave energy converters (OSWECs) in this paper due to its high capacity for industrialization [24].

Over the past two decades, a number of studies have been conducted to understand how OSWECs' structures and interactions between ocean waves and flaps affect converters performance. Henry et al.'s experiment on oscillating surge wave energy converters is considered as one of the most influential pieces of research [25], which demonstrated how the performance of oscillating surge wave energy converters (OSWECs) is affected by seven different factors, including wave period, wave power, flap's relative density, water depth, free-board of the flap, the gap between the tubes, gap underneath the flap, and flap width. These parameters were assessed in their two models in order to estimate the absorbed energy from incoming waves [26,27]. In addition, Folly et al. investigated the impact of water depth on the OSWECs performance analytically, numerically, and experimentally. According to this and further similar studies, the average annual incident wave power is significantly reduced by water depth. Based on the experimental results, both the surge wave force and the power capture of OSWECs increase in shallow water [28,29]. Following this, Sarkar et al. found that under such circumstances, the device that is located near the coast performs much better than those in the open ocean [30]. On the other hand, other studies are showing that the size of the converter, including height and width, is relatively independent of the location (within similar depth) [31]. Subsequently, Schmitt et al. studied OSWECs numerically and experimentally. In fact, for the simulation of OSWEC, OpenFOAM was used to test the applicability of Reynolds-averaged Navier-Stokes (RANS) solvers. Then, the experimental model reproduced the numerical results with satisfying accuracy [32]. In another influential study, Wang et al. numerically assessed the effect of OSWEC's width on their performance. According to their findings, as converter width increases, its efficiency decreases in short wave periods while increases in long wave periods [33]. One of the main challenges in the analysis of the OSWEC is the coupled effect of hydrodynamic and geometric variables. As a result, numerous cutting-edge geometry studies have been performed in recent years in order to find the optimal structure that maximizes power output and minimizes costs. Garcia et al. reviewed hull geometry optimization studies in the literature in [19]. In addition, Guo and Ringwood surveyed geometric optimization methods to improve the hydrodynamic performance of OSWECs at the primary stage [14]. Besides, they classified the hull geometry of OSWECs based on Fig. 1. Subsequently, Whittaker et al. proposed a different design of OSWEC called Oyster2. There have been three examples of different geometries of oysters with different water depths. Based on its water depth, they
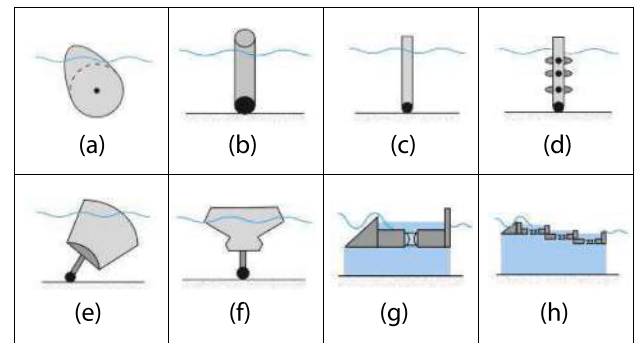

Fig. 1. Different designs of fixed and floating OSWECs [14].

determined the width and height of the converter. They also found that in the constant wave period the less the converter's width, the less power captures the converter has [34]. Afterward, O'Boyle et al. investigated a type of OSWEC called Oyster 800. They compared the experimental and numerical models with the prototype model. In order to precisely reproduce the shape, mass distribution, and buoyancy properties of the prototype, a 40th-scale experimental model has been designed. Overall, all the models were fairly accurate according to the results [35].

Inclusive analysis of recent research avenues in the area of flap geometry has revealed that the interaction-based designs of such converters are emerging as a novel approach. An initiative workflow is designed in the current study to maximizing the wave energy extrication by such systems. To begin with, a sensitivity analysis plays its role of determining the best hydrodynamic values for installing the converter's flap. Then, all flap dimensions and characteristics come into play to finalize the primary model. Following, interactive designs is proposed to increase the influence of incident waves on the body by adding ribs on both sides of the flap as a novel design. Finally, a new bi-level meta-heuristic method is proposed to consider the effects of simultaneous changes in ribs properties and other design parameters. We hope this novel approach will be utilized to make big-scale projects less costly and justifiable. The efficiency of the method is also compared with four well known metaheuristic algorithms and out weight them for this application.

This paper is organized as follows. First, the research methodology is introduced by providing details about the numerical model implementation. To that end, we first introduced the primary model's geometry and software details. That primary model is later verified with a benchmark study with regard to the flap angle of rotation and water surface elevation. Then, governing equations and performance criteria are presented. In the third part of the paper, we discuss the model's sensitivity to lower and upper parts width (we proposed a two cross-sectional design for the flap), bottom elevation, and freeboard. Finally, the novel optimization approach is introduced in the final part and compared with four recent metaheuristic algorithms.

2. Numerical methods

In this section, after a brief introduction of the numerical software, Flow3D, boundary conditions are defined. Afterwards, the numerical model implementation, along with primary model properties are described. Finally, governing equations, as part of numerical process, are discussed.

2.1. Model setup

FLOW-3D is a powerful and comprehensive CFD simulation platform for studying fluid dynamics. This software has several modules to solve many complex engineering problems. In addition, modeling complex flows is simple and effective using FLOW-3D's robust meshing

capabilities [36]. Interaction between fluid and moving objects might alter the computational range. Dynamic meshes are used in our modeling to take these changes into account. At each time step, the computational node positions change in order to adapt the meshing area to the moving object. In addition, to choose mesh dimensions, some factors are taken into account such as computational accuracy, computational time, and stability. The final grid size is selected based on the detailed procedure provided in [37]. To that end, we performed grid-independence testing on a CFD model using three different mesh grid sizes of 0.01, 0.015, and 0.02 m. The problem geometry and boundary conditions were defined the same, and simulations were run on all three grids under the same conditions. The predicted values of the relevant variable, such as velocity, was compared between the grids. The convergence behavior of the numerical solution was analyzed by calculating the relative L2 norm error between two consecutive grids. Based on the results obtained, it was found that the grid size of 0.02 m showed the least error, indicating that it provided the most accurate and reliable solution among the three grids. Therefore, the grid size of 0.02 m was selected as the optimal spatial resolution for the mesh grid.

In this work, the flume dimensions are 10 m long, 0.1 m wide, and 2.2 m high, which are shown in Fig. 2. In addition, input waves with linear characteristics have a height of 0.1 m and a period of 1.4 s. Among the linear wave methods included in this software, RNGk-ε and k- ε are appropriate for turbulence model. The research of Lopez et al. shows that RNGk- ε provides the most accurate simulation of turbulence in OSWECs [21]. We use CATIA software to create the flap primary model and other innovative designs for this project. The flap measures 0.1 m × 0.65 m × 0.360 m in ×, y and z directions, respectively. In Fig. 3, the primary model of flap and its dimensions are shown. In this simulation, five boundaries have been defined, including 1. Inlet, 2. Outlet, 3. Converter flap, 4. Bed flume, and 5. Water surface, which are shown in Fig. 2. Besides, to avoid wave reflection in inlet and outlet zones, Flow3D is capable of defining some areas as damping zones, the length of which has to be one to one and a half times the wavelength. Therefore, in the model, this length is considered equal to 2 m. Furthermore, there is no slip in all the boundaries. In other words, at every single time step, the fluid velocity is zero on the bed flume, while it is equal to the flap velocity on the converter flap. According to the wave theory defined in the software, at the inlet boundary, the water velocity is called from the wave speed to be fed into the model.

2.2. Verification

In the current study, we utilize the Schmitt experimental model as a benchmark for verification, which was developed at the Queen's University of Belfast. The experiments were conducted on the flap of the converter, its rotation, and its interaction with the water surface. Thus, the details of the experiments are presented below based up on the experimental setup's description [38]. In the experiment, the laboratory flume has a length of 20 m and a width of 4.58 m. Besides, in order to avoid incident wave reflection, a wave absorption source is devised at the end of the left flume. The flume bed, also, includes two parts with different slops. The flap position and dimensions of the flume can be seen in Fig. 4. In addition, a wave-maker with 6 paddles is installed at

one end. At the opposite end, there is a beach with wire meshes. Additionally, there are 6 indicators to extract the water level elevation. In the flap model, there are three components: the fixed support structure, the hinge, and the flap. The flap measures 0.1 m × 0.65 m × 0.341 m in x, y and z directions, respectively. In Fig. 5, the details are given [32]. The support structure consists of a 15 mm thick stainless steel base plate measuring 1 m by 1.4 m, which is screwed onto the bottom of the tank. The hinge is supported by three bearing blocks. There is a foam centerpiece on the front and back of the flap which is sandwiched between two PVC plates. Enabling changes of the flap, three metal fittings link the flap to the hinge. Moreover, in this experiment, the selected wave is generated based on sea wave data at scale 1:40. The wave height and the wave period are equal to 0.038 (m) and 2.0625 (s), respectively, which are tantamount to a wave with a period of 13 (s) and a height of 1.5 (m).

Two distinct graphs illustrate the numerical and experi-mental study results. Fig. 6 and Fig. 7 are denoting the angle of rotation of flap and surface elevation in computational and experimental models, respectively. The two figures roughly represent that the numerical and experimental models are a good match. However, for the purpose of verifying the match, we calculated the correlation coefficient (C) and root mean square error (RMSE). According to Fig. 6, correlation coefficient and RMSE are 0.998 and 0.003, respectively, and in Fig. 7 correlation coefficient and RMSE are respectively 0.999 and 0.001. Accordingly, there is a good match between the numerical and empirical models. It is worth mentioning that the small differences between the numerical and experimental outputs may be due to the error of the measuring devices and the calibration of the data collection devices.

Including continuity equation and momentum conserva- tion for incompressible fluid are given as [32,39]:

$$\frac{\partial}{\partial x_j}(u_i) = 0 \qquad (1)$$

$$\frac{\partial}{\partial t}(u_i) + \frac{\partial}{\partial x_j}(u_j u_i) = \frac{1}{\rho}\frac{\partial P}{\partial x_j} +$$
$$\frac{1}{\rho}\frac{\partial}{\partial x_j}[\mu_{eff}(\frac{\partial u_j}{\partial x_i} + \frac{\partial u_i}{\partial x_j})] - D_i u_i + g_i \qquad (2)$$

where P represents the pressure, g denotes gravitational acceleration, u represents fluid velocity, and *Di* is damping coefficient. Likewise, the model uses the same equation to calculate the fluid velocity in other directions as well. Considering the turbulence, we use the two-equation model of RNGK- ε. These equations are:

$$\frac{\partial}{\partial t}(\rho k) + \frac{\partial}{\partial x_j}(\rho u_j k) = \frac{\partial}{\partial x_j}[\mu_{eff}\alpha_k \frac{\partial k}{\partial x_j}] + P_k - \rho\varepsilon \qquad (3)$$

and

$$\frac{\partial}{\partial t}(\rho\varepsilon) + \frac{\partial}{\partial x_j}(\rho u_j \varepsilon) = \frac{\partial}{\partial x_j}[\mu_{eff}\alpha_e \frac{\partial \varepsilon}{\partial x_j}] + C_{1\varepsilon}^* P_k \frac{\varepsilon}{k} - \rho C_{2\varepsilon}\frac{\varepsilon^2}{k} \qquad (4)$$

where $C_{2\varepsilon}$ and $C_{1\varepsilon}$ are constants. In addition, α_ε and α_k represent the turbulent Prandtl number of ε and k, respectively.

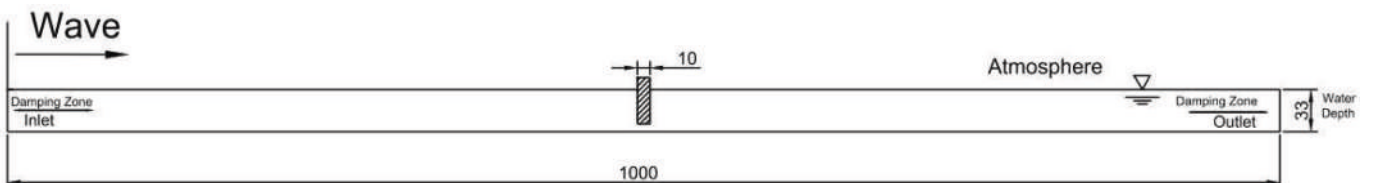P_k also denote the production of turbulent kinetic energy of k under

devices.

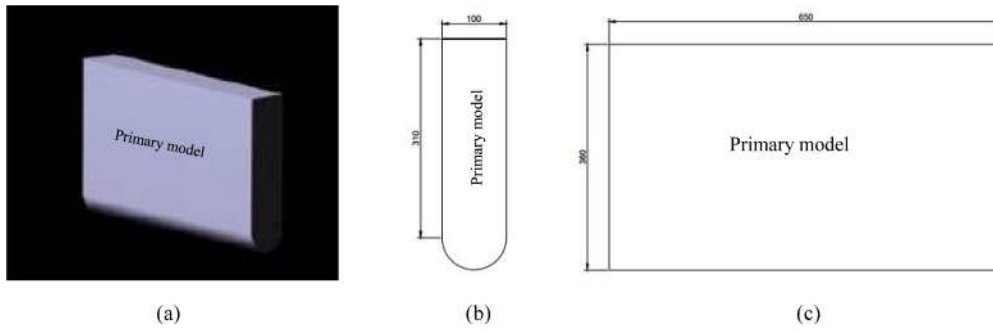**Fig. 2.** Boundary conditions and waves damping zone in flume.

Fig. 3. Flap primary model in CATIA software (a) flap primary model 3D view (b) flap primary model side view (c) flap primary model front view factor equations are applied. RANS equations.
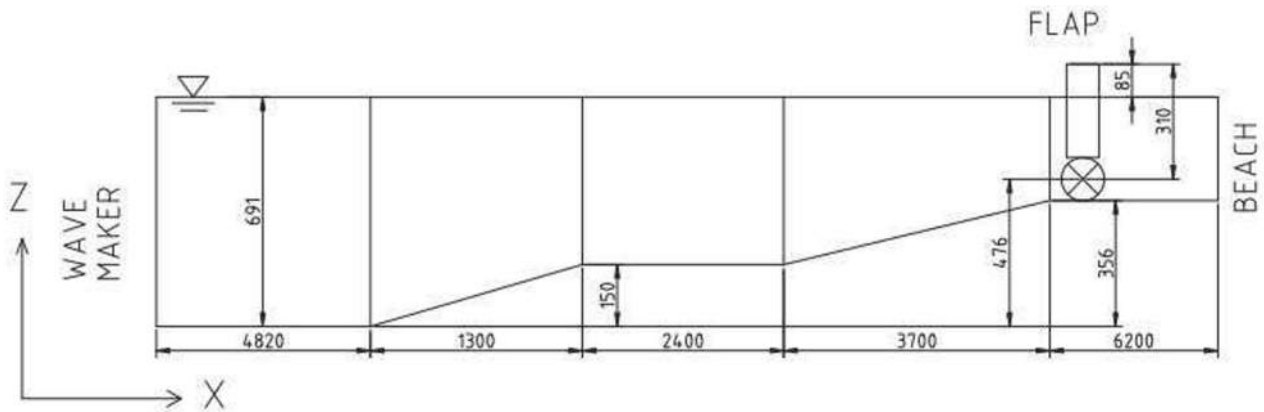

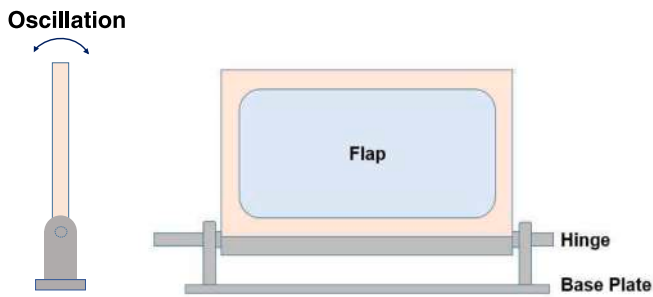**Fig. 4.** Diagram of flume, water level, and flap position. Dimensions are in millimeters [32].

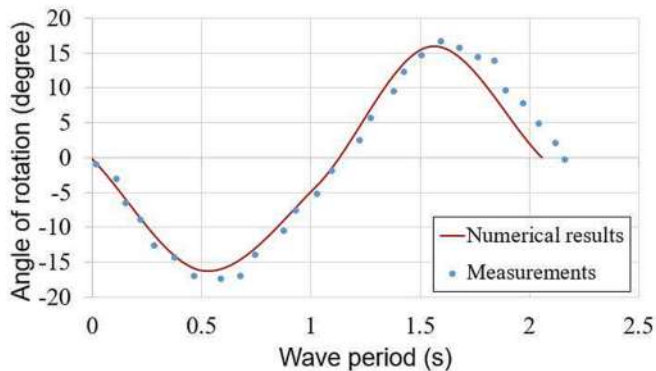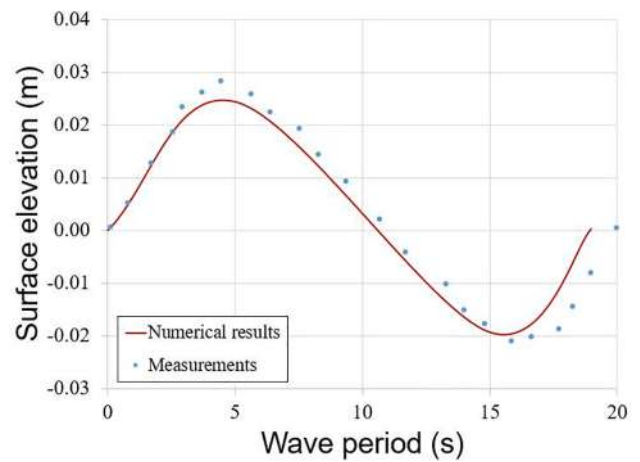**Fig. 5.** Schematic view of flap and support structure [32].

Fig. 7. Comparing surface elevation in computational and experimental model.

the effect of velocity gradient, which is calculated as follows:

$$P_k = \mu_{eff}[\frac{\partial u_i}{x_j} + \frac{\partial u_j}{x_i}] \ \frac{\partial u_i}{x_j} \tag{5}$$

$$\mu_{eff} = \mu + \mu_f \tag{6}$$

$$\mu_{eff} = \mu + \mu_f \tag{7}$$

where μ is molecular viscosity, μf represents turbulence viscosity, k denotes kinetic energy, and ϵ is energy dissipation rate. The values of constant coefficients in the two-equation RNGK $-\epsilon$ model is as shown in

Fig. 6. Comparing the angle of rotation of flap in computational and experimental model.

the Table 1 [40].

It is worth mentioning that the volume of fluid method is used to separate water and air phases in this software [41]. Below is the equation of this method [40].

$$\frac{\partial \alpha}{\partial t} + \frac{\partial}{\partial x_j}(u_i \alpha) = 0 \tag{8}$$

where α and $1 - \alpha$ are portion of water phase and air phase, respectively. As a weighting factor, each fluid phase portion is used to determine the mixture properties. Finally, using the following equations, we calculate the efficiency of converters [42,34,43]:

$$P = \frac{1}{4} \frac{|F|^2}{B + \sqrt{B^2 + (I + I_a)^2(\omega_n^2 - \omega^2)^2}} \tag{9}$$

where ω_n represents natural frequency, I denotes the inertia of OSWEC, Ia is the added inertia, F is the complex wave force, and B denotes the hydrodynamic damping coefficient. Afterward, the capture factor of the converter is calculated by [44]:

$$C_F = \frac{P}{(1/2)A_I^2 C_g w} \tag{10}$$

C_{gw} where C_f represents the capture factor, which is the total efficiency of device per unit length of the wave crest at each time step [15], A_I represent the dimensional amplitude of the incident wave, w is the flap's width, and Cg is the group velocity of the incident wave, as below:

$$C_g = \frac{\omega}{k_0} \cdot \frac{1}{2}\left[1 + \frac{2k_0 h}{\sinh(2k_0 h)}\right] \tag{11}$$

where $k0$ denotes the wave number, h is water depth, and H is the height of incident waves.

According to previous sections , $RNGK - \epsilon$ modeling is used for all models simulated in this section. For this purpose, the empty boundary condition is used for flume walls. In order to preventing wave reflection at the inlet and outlet of the flume, the length of wave absorption is set to be at least one incident wavelength. In addition, the structured mesh is chosen, and the mesh dimensions are selected in two distinct directions. In each model, all grids have a length of 2 (cm) and a height of 1 (cm). Afterwards, as an input of the software for all of the models, we define the time step as 0.001 (s). Moreover, the run time of every simulation is 30 (s). As mentioned before, our primary model is Schmitt model, and the flap properties is given in Table 2. For all simulations, the flume measures 15 m in length and 0.65 m in width, and water depth is equal to 0.335 (m). The flap is also located 7 m from the flume's inlet.

Finally, in order to compare the results, the capture factor is calculated for each simulation and compared to the primary model. It is worth mentioning that capture factor refers to the ratio of absorbed wave energy to the input wave energy.

According to primary model simulation and due to the decreasing horizontal velocity with depth, the wave crest has the highest velocity. Considering the fact that the wave's orbital velocity causes the flap to move, the contact between the upper edge of the flap and the incident wave can enhance its performance. Additionally, the numerical model shows that the dynamic pressure decreases as depth increases, and the hydrostatic pressure increases as depth increases.

To determine the OSWEC design, it is imperative to understand the correlation between the capture factor, wave period, and wave height. Therefore, as it is shown in Fig. 8, we plot the change in capture factor

Table 1
Constant coefficients in RNGK-∈ model.

Factors	β	η_0	C_1	C_2	α_e	α_k	C_μ
Quantity	0.012	4.38	1.42	1.68	1.39	1.39	0.084

Table 2
Flap properties.

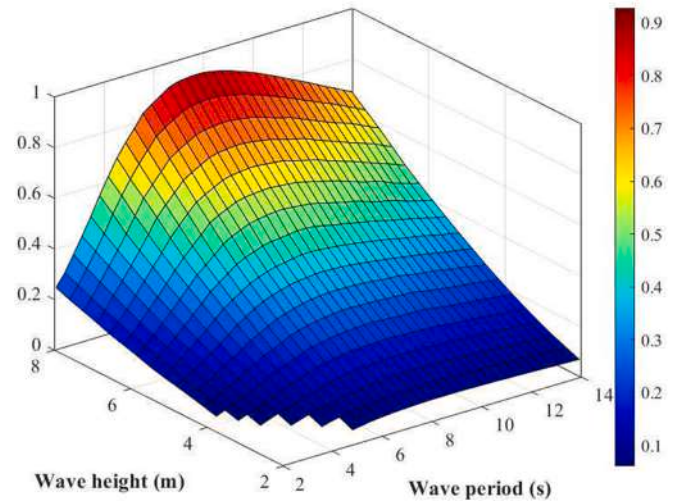|	
Joint height (m)	0.476
Height of the center of mass (m)	0.53
Weight (Kg)	10.77

Fig. 8. OSWEC's capture factor changes with incident wave periods and heights.

over the variations in wave period and wave height in 3D and 2D. In this diagram, the first axis features changes in wave period, the second axis displays changes in wave height, and the third axis depicts changes in capture factor. According to our wave properties in the numerical model, the wave period and wave height range from 2 to 14 s and 2 to 8 m, respectively. This is due to the fact that the flap does not oscillate if the wave height is less than 2 (m), and it does not reverse if the wave height is more than 8 (m). In addition, with wave periods more than 14 (s), the wavelength would be so long that it would violate the deep-water conditions, and with wave periods less than 2 (s), the flap would not oscillate properly due to the shortness of wavelength. The results of simulation are shown in Fig. 8. As it can be perceived from Fig. 8, in a constant wave period, the capture factor is in direct proportion to the wave height. It is because of the fact that waves with more height have more energy to rotate the flap. Besides, in a constant wave height, the capture factor increases when the wave period increases, until a given wave period value. However, the capture factor falls after this point. These results are expected since the flap's angular displacement is not high in lower wave periods, while the oscillating motion of that is not fast enough to activate the power take-off system in very high wave periods.

As is shown in Fig. 9, we plot the change in capture factor over the variations in wave period (s) and water depth (m) in 3D. As it can be seen in this diagram, the first axis features changes in water depth (m), the second axis depicts the wave period (s), and the third axis displays OSWEC's capture factor. The wave period ranges from 0 to 10 s based on our wave properties, which have been adopted from Schmitt's model, while water depth ranges from 0 to 0.5 m according to the flume and flap dimensions and laboratory limitations. According to Fig. 9, for any specific water depth, the capture factor increases in a varying rate when the wave period increases, until a given wave period value. However, the capture factor falls steadily after this point. In fact, the maximum capture factor occurs when the wave period is around 6 s. This trend is expected since, in a specific water depth, the flap cannot oscillate properly when the wavelength is too short. As the wave period increases, the flap can oscillate more easily, and consequently its capture factor
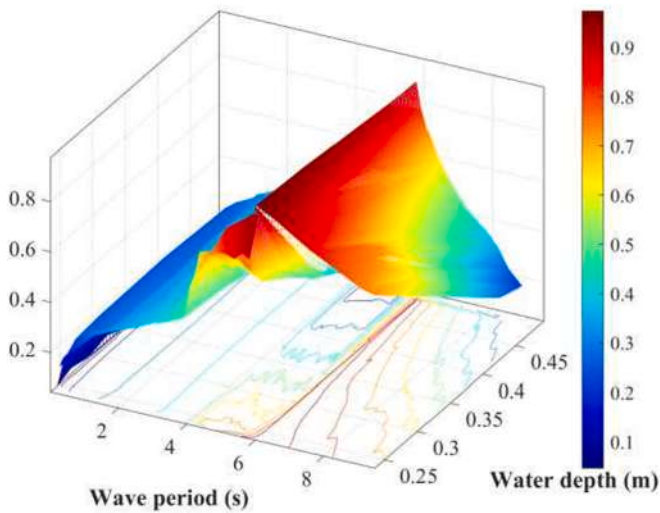
Fig. 9. Tracing the effect of changes in wave period and depth on the OSWEC's capture factor. The color bar represents capture factor values.

increases. However, the capture factor drops in higher wave periods because the wavelength is too large to move the flap. Furthermore, in a constant wave period, by changing the water depth, the capture factor does not alter. In other words, the capture factor does not depend on the water depth when it is around its maximum value.

3. Sensitivity analysis

Based on previous studies, in addition to the flap design, the location of the flap relative to the water surface (freeboard) and its elevation relative to the flume bed (flap bottom elevation) play a significant role in extracting energy from the wave energy converter. This study measures the sensitivity of the model to various parameters related to the flap design including upper part width of the flap, lower part width of the flap, the freeboard, and the flap bottom elevation. Moreover, as a novel idea, we propose that the flap widths differ in the lower and upper parts. In Fig. 10, as an example, a flap with an upper thickness of 100 (mm) and a lower thickness of 50 (mm) and a flap with an upper thickness of 50 (mm) and a lower thickness of 100 (mm) are shown. The influence of such discrepancy between the widths of the upper and lower parts on the interaction between the wave and the flap, or in other words on the capture factor, is evaluated. To do so, other parameters are remained constant, such as the freeboard, the distance between the flap and the flume bed, and the wave properties.
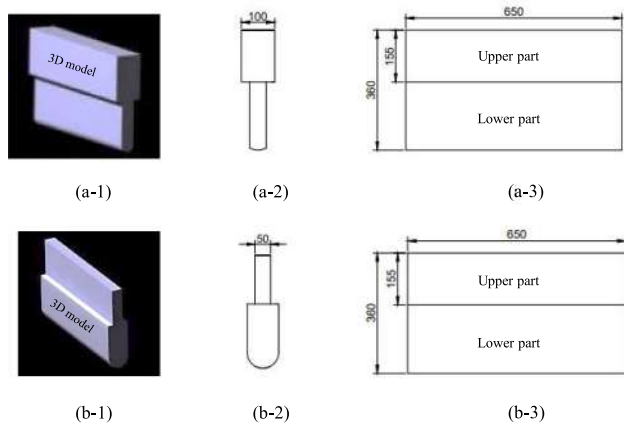
In Fig. 11, models are simulated with distinct upper and lower widths. As it is clear in this figure, the first axis depicts the lower part width of the flap, the second axis indicates the upper part width of the flap, and the colors represent the capture factor values. Additionally, in order to consider a sufficient range of change, the flap thickness varies from half to double the value of the primary model for each part.

According to this study, the greater the discrepancy in these two parts, the lower the capture factor. It is on account of the fact that when the lower part of the flap is thicker than the upper part, and this thickness difference in these two parts is extremely conspicuous, the inertia against the motion is significant at zero degrees of rotation. Consequently, it is difficult to move the flap, which results in a low capture factor. Similarly, when the upper part of the flap is thicker than the lower part, and this thickness difference in these two parts is exceedingly noticeable, the inertia is so great that the flap cannot reverse at the maximum degree of rotation. As the results indicate, the discrepancy can enhance the performance of the converter if the difference between these two parts is around 20%. As it is depicted in the Fig. 11, the capture factor reaches its own maximum amount, when the lower part thickness is from 5 to 6 (cm), and the upper part thickness is between 6 and 7 (cm). Consequently, as a result of this discrepancy, less material will be used, and therefore there will be less cost.

As illustrated in Fig. 12, this study examines the effects of freeboard (level difference between the flap top and water surface) and the flap bottom elevation (the distance between the flume bed and flap bottom) on the converter performance. In this diagram, the first axis demonstrates the freeboard and the second axis on the left side displays the flap bottom elevation, while the colors indicate the capture factor. In addition, the feasible range of freeboard is between −15 to 15 (cm) due to the limitation of the numerical model, so that we can take the wave slamming and the overtopping into consideration. Additionally, based on the Schmitt model and its scaled model of 1:40 of the base height, the flap bottom should be at least 9 (cm) high. Since the effect of surface waves is distributed over the depth of the flume, it is imperative to maintain a reasonable flap height exposed to incoming waves. Thus, the maximum flap bottom elevation is limited to 19 (cm). As the Fig. 12 pictures, at constant negative values of the freeboard, the capture factor is in inverse proportion with the flap bottom elevation, although slightly.

Fig. 10. Dimensions of the flap with different widths. (a): Three dimensional and side views of a flap with thicker upper half, (b): Three dimensional and side views of a flap with thicker lower half.
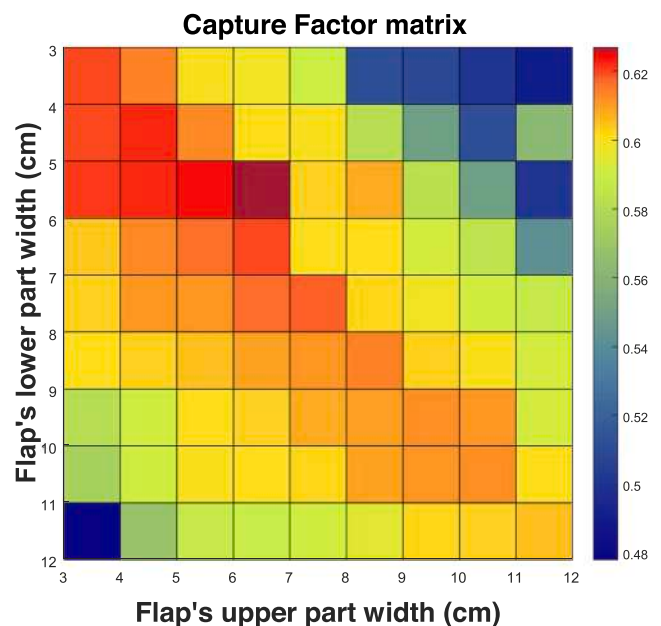

Fig. 11. Effects of changes in the flap thickness in lower and upper parts on the capture factor of OSWEC.
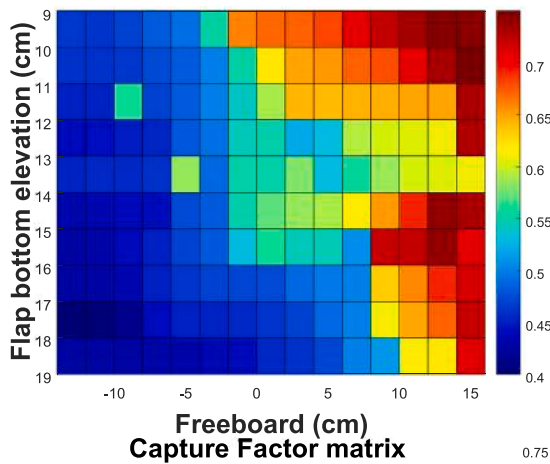
Fig. 12. Effects of changes in flap displayed bottom elevation on the Capture factor.

Fig. 14. Flow velocity field around the WEC flap (side view).

Furthermore, at constant positive values of the freeboard, the capture factor fluctuates as the flap bottom elevation decreases while it maintains an overall increasing trend. This is on account of the fact that increasing the flap bottom elevation creates turbulence flow behind the flap, which encumbers its rotation, as well as the fact that the flap surface has less interaction with the incoming waves. Furthermore, while keeping the flap bottom elevation constant, the capture factor increases by raising the freeboard. This is due to the fact that there is overtopping with adverse impacts on the converter performance when the freeboard is negative and the flap is under the water surface. Besides, increasing the freeboard makes the wave slam more vigorously, which improves the converter performance.

Adding ribs to the flap surface, as shown in Fig. 13, is a novel idea that is investigated in the next section. To achieve an optimized design for the proposed geometry of the flap, we determine the optimal number and dimensions of ribs based on the flap properties as our decision variables in the optimization process. As an example, Fig. 13 illustrates a flap with 3 ribs on each side with specific dimensions.

Fig. 14 shows the flow velocity field around the flap jointed to the flume bed. During the oscillation of the flap, the pressure on the upper and lower surfaces of the flap changes dynamically due to the changing angle of attack and the resulting change in the direction of fluid flow. As the flap moves upwards, the pressure on the upper surface decreases, and the pressure on the lower surface increases. Conversely, as the flap moves downwards, the pressure on the upper surface increases, and the pressure on the lower surface decreases. This results in a cyclic pressure variation around the flap. Under certain conditions, the pressure field around the flap can exhibit significant variations in magnitude and direction, formin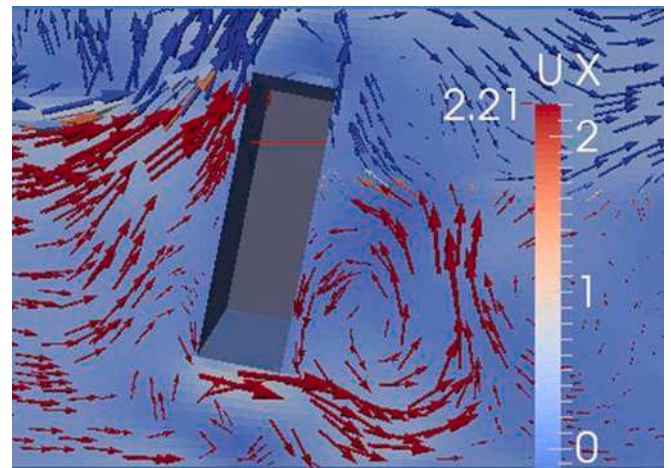g vortices and other flow structures. These flow structures can affect the performance of the OSWEC by altering the lift and drag forces acting on the flap.

4. Design optimization

We consider optimizing the design parameters of the flap of converter using a nature-based swarm optimization method, that fall in the category of metaheuristic algorithms [45]. Accordingly, we choose four state-of-the-art algorithms to perform an optimization study. Then, based on their performances to achieve the highest capture factor, one of them will be chosen to be combined with the Hill Climb algorithm to carry out a local search. Therefore, in the remainder of this section, we discuss the search process of each algorithm and visualize their performance and convergence curve as they try to find the best values for decision variables.

4.1. Metaheuristic approaches

As the first considered algorithm, the Gray Wolf Optimizer (GWO) algorithm simulates the natural leadership and hunting performance of gray wolves which tend to live in colonies. Hunters must obey the alpha wolf, the leader, who is responsible for hunting. Then, the beta wolf is at the second level of the gray wolf hierarchy. A subordinate of alpha wolf, beta stands under the command of the alpha. At the next level in this hierarchy, there are the delta wolves. They are subordinate to the alpha and beta wolves. This category of wolves includes scouts, sentinels, elders, hunters, and caretakers. In this ranking, omega wolves are at the bottom, having the lowest level and obeying all other wolves. They are also allowed to eat the prey just after others have eaten. Despite the fact
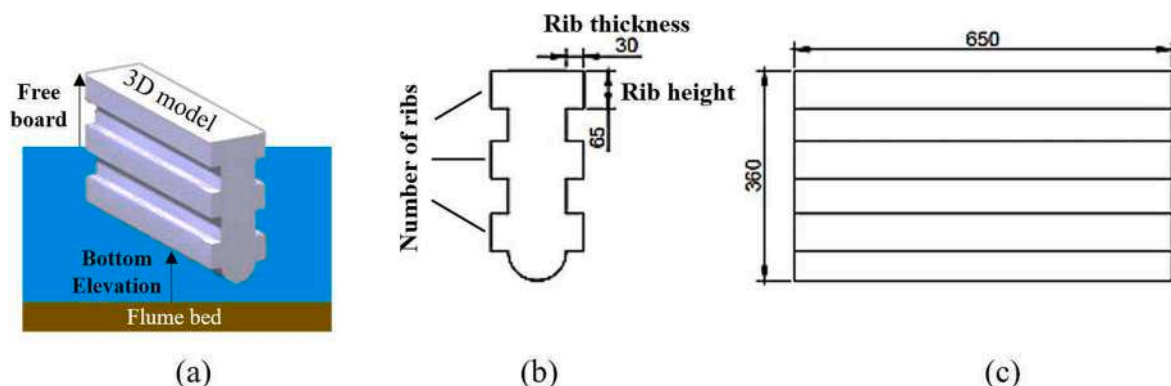

Fig. 13. 3D view (a) and 2D side views (b,c) of the flap of OSWEC with three added ribs, the optimal number of ribs are.

that they seem less important than others, they are really central to the pack survival. Since, it has been shown that without omega wolves, the entire pack would experience some problems like fighting, violence, and frustration. In this simulation, there are three primary steps of hunting including searching, surrounding, and finally attacking the prey. Mathematically model of gray wolves' hunting technique and their social hierarchy are applied in determined by optimization this study. As mentioned before, gray wolves can locate their prey and surround them. The alpha wolf also leads the hunt. Assuming that the alpha, beta, and delta have more knowledge about prey locations, we can mathematically simulate gray wolf hunting behavior. Hence, in addition to saving the top three best solutions obtained so far, we compel the rest of the search agents (also the omegas) to adjust their positions based on the best search agent. Encircling behavior can be mathematically modeled by the following equations: [46].

$$\vec{D} = |\vec{C} \cdot \vec{X_p}(t) - \vec{X}(t)| \tag{12}$$

$$\vec{X}(t+1) = \vec{X_p}(t) - \vec{A} \cdot \vec{D} \tag{13}$$

$$\vec{C} = 2 \cdot \vec{r_2} \tag{14}$$

$$\vec{A} = 2\vec{a} \cdot \vec{r_1} - \vec{a} \tag{15}$$

where $\vec{X}$ indicates the position vector of gray wolf, $\vec{X_p}$ defines the vector of prey, t indicates the current iteration, and $\vec{A}$ and $\vec{C}$ are coefficient vectors. To force the search agent to diverge from the prey, we use $\vec{A}$ with random values greater than 1 or less than -1. In addition, $C \rightarrow$ contains random values in the range [0,2], and $\vec{r}_1$ and $\vec{r_2}$ are random vectors in [0,1]. The second considered technique is the Moth Flame Optimizer (MFO) algorithm. This method revolves around the moths' navigation mechanism, which is realized by positioning themselves and maintaining a fixed angle relative to the moon while flying. This effective mechanism helps moths to fly in a straight path. However, when the source of light is artificial, maintaining an angle with the light leads to a spiral flying path towards the source that causes the moth's death [47]. In MFO algorithm, moths and flames are both solutions. The moths are actual search agents that fly in hyper-dimensional space by changing their position vectors, and the flames are considered pins that moths drop when searching the search space [48]. The problem's variables are the position of moths in the space. Each moth searches around a flame and updates it in case of finding a better solution. The fitness value is the return value of each moth's fitness (objective) function. The position vector of each moth is passed to the fitness function, and the output of the fitness function is assigned to the corresponding moth. With this mechanism, a moth never loses its best solution [49]. Some attributes of this algorithm are as follows:

- It takes different values to converge moth in any point around the flame.
- Distance to the flame is lowered to be eventually minimized.
- When the position gets closer to the flame, the updated positions around the flame become more frequent.

As another method, the Multi-Verse Optimizer is based on a multiverse theory which proposes there are other universes besides the one in which we all live. According to this theory, there are more than one big bang in the universe, and each big bang leads to the birth of a new universe [50]. Multi-Verse Optimizer (MVO) is mainly inspired by three phenomena in cosmology: white holes, black holes, and wormholes. A white hole has never been observed in our universe, but physicists believe the big bang could be considered a white hole [51]. Black holes, which behave completely in contrast to white holes, attract everything including light beams with their extremely high gravitational force [52]. In the multiverse theory, wormholes are time and space tunnels that

allow objects to move instantly between any two corners of a universe (or even simultaneously from one universe to another) [53]. Based on these three concepts, mathematical models are designed to perform exploration, exploitation, and local search, respectively. The concept of white and black holes is implied as an exploration phase, while the concept of wormholes is considered as an exploitation phase by MVO. Additionally, each solution is analogous to a universe, and each variable in the solution represents an object in that universe. Furthermore, each solution is assigned an inflation rate, and the time is used instead of iterations. Following are the universe rules in MVO:

- The possibility of having white hole increases with the inflation rate.
- The possibility of having black hole decreases with the inflation rate.
- Objects tend to pass through black holes more frequently in universes with lower inflation rates.
- Regardless of inflation rate, wormholes may cause objects in universes to move randomly towards the best universe [54]

Modeling the white/black hole tunnels and exchanging objects of universes mathematically was accomplished by using the roulette wheel mechanism. With every iteration, the universes are sorted according to their inflation rates, then, based on the roulette wheel, the one with the white hole is selected as the local extremum solution. This is accomplished through the following steps:

Assume that

$$x_i^j = \begin{cases} x_k^j & r1 < NI(Ui) \\ x_i^j r1 \geq NI(Ui) \end{cases} \tag{16}$$

Where x_i^j represents the jth parameter of the ith universe, Ui indicates the ith universe, NI(Ui) is normalized inflation rate of the ith universe, r1 is a random number in [0,1], and $j x_k$ shows the jth parameter of the kth universe selected by a roulette wheel selection mechanism [54]. It is assumed that wormhole tunnels always exist between a universe and the best universe formed so far. This mechanism is as follows:

$$x_i^j = \begin{cases} \begin{cases} if r_2 < WEP : \\ X_j + \\ TDR \times ((ub_j - lb_j) \times r_4 + lb_j) & r_3 < 0.5 \\ X_j - \\ TDR \times ((ub_j - lb_j) \times r_4 + lb_j) & r_3 \geq 0.5 \\ else : x_i^j \end{cases} \end{cases} \tag{17}$$

where Xj indicates the jth parameter of the best universe formed so far, TDR and WEP are coefficients, where Xj indicates the jth parameter of the best *universelbjshows* the lower bound of the jth variable, *ubj* is the upper bound of the jth variable, and r2, r3, and r4 are random numbers in [0,1] [54].

Finally, one of the newest optimization algorithms is WOA. The WOA algorithm simulates the movement of prey and the whale's discipline when looking for their prey. Among several species, Humpback whales have a specific method of hunting [55]. Humpback whales can recognize the location of prey and encircle it before hunting. The optimal design position in the search space is not known a priori, and the WOA algorithm assumes that the best candidate solution is either the target prey or close to the optimum. This foraging behavior is called the bubble-net feeding method. Two maneuvers are associated with bubbles: upward spirals and double loops. A unique behavior exhibited only by humpback whales is bubble-net feeding. In fact, The WOA algorithm starts with a set of random solutions. At each iteration, search agents update their positions for either a randomly chosen search agent or the best solution obtained so far [56,55]. When the best search agent is determined, the other search agents will attempt to update their positions toward that agent. It is important to note that humpback whales swim

around their prey simultaneously in a circular, shrinking circle and along a spiral-shaped path. By using a mathematical model, the spiral bubble-net feeding maneuver is optimized. The following equation represents this behavior:

$$\overrightarrow{X}(t+1) = \overrightarrow{D'} \cdot e^{bl} \cdot \cos(2\pi l) + \overrightarrow{X^*}(t) \tag{18}$$

where:

$$\overrightarrow{D'} = |\overrightarrow{X^*}(t) - \overrightarrow{X}(t)| \tag{19}$$

$\overrightarrow{X}_{(t+1)}$ indicates the distance of the $it\,h$ whale to the prey (best solution obtained so far),b is a constant for defining the shape of the logarithmic spiral, l is a random number in $[-1,\, 1]$, and dot (.) is an element-by-element multiplication [55].

Comparing the four above-mentioned methods, simulations are run with 10 search agents for 400 iterations. In Fig. 15, there are 20 plots the optimal values of different parameters in optimization algorithms. The five parameters of this study are freeboard, bottom elevations, number of ribs on the converter, rib thickness, and rib Height. The optimal value for each was found by optimization algorithms, naming WOA, MVO, MFO, and GWO. By looking through the first row, the freeboard parameter converges to its maximum possible value in the optimization process of GWO after 300 iterations. Similarly, MFO finds the same result as GWO. In contrast, the freeboard converges to its minimum possible value in MVO optimizing process, which indicates positioning the converter under the water. Furthermore, WOA found the optimal

value of freeboard as around 0.02 after almost 200 iterations. In the second row, the bottom elevation is found at almost 0.11 (m) in all algorithms; however, the curves follow different trends in each algorithm. The third row shows the number of ribs, where results immediately reveal that it should be over 4. All algorithms coincide at 5 ribs as the optimal number in this process. The fourth row displays the trends of algorithms to find optimal rib thickness. MFO finds the optimal value early and sets it to around 0.022, while others find the same value in higher iterations. Finally, regarding the rib height, MVO, MFO, and GWO state that the optimal value is 0.06 m, but WOA did not find a higher value than 0.039.

4.2. HCMVO Bi-level approach

Despite several strong search characteristics of MVO and its high performance in various optimization problems, it suffers from a few deficiencies in local and global search mechanisms. For instance, it is trapped in the local optimum when wormholes stochastically generate many solutions near the best universe achieved throughout iterations, especially in solving complex multimodal problems with high dimensions [57]. Furthermore, MVO needs to be modified by an escaping strategy from the local optima to enhance the global search abilities. To address these shortages, we propose a fast and effective *meta*-algorithm (HCMVO) to combine MVO with a Random-restart hill-climbing local search. This *meta*-algorithm uses MVO on the upper level to develop global tracking and provide a range of feasible and proper solutions. The hill-climbing algorithm is designed to develop a comprehensive
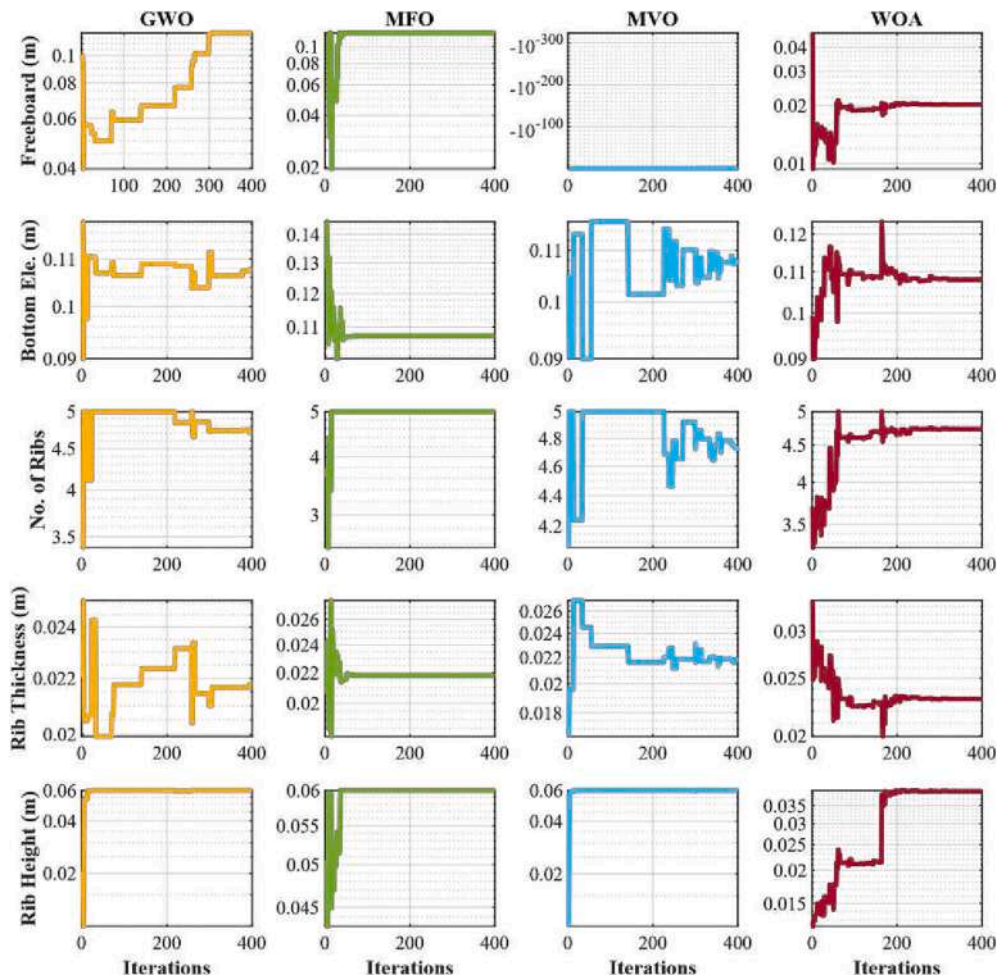

Fig. 15. Tracing the change of freeboard (first row), bottom elevation (second row), number of ribs (third row), rib thickness (forth row), and rib height (fifth row) by each optimization method.

neighborhood search around the best-found solution proposed by the upper-level (MVO) when MVO is faced with a stagnation issue or falling into a local optimum. The performance threshold is formulated as follows.

Algorithm 1: *Hill Climb Multiverse Optimization*	
01:	procedure HCMVO
02:	$N = 30$, $M = 5$▷*Population size and performance index*
03:	$\mathbb{S} = \{\langle F_1, B_1, N, R, H_1\rangle, ... \langle F_N, B_2, N, R, H_N\rangle\} \Rightarrow \text{lb}_1^N \leqslant \mathbb{S} \leqslant \text{ub}^N$
04:	Initialize parameters W_{ER}, T_{DR}, W_{EP}, Best $_u$,Max_{iter_N}▷ Wormhole existence probability (WEP)
05:	$S_U = sort(S_i)$
06:	$N_I = $ Normalize the inflation rate S_I
07:	for iter in $[1,···,Max_{iter}]$ do
08:	for i in $[1,···,N]$ do
09:	Update W_{EP}, T_{DR}, Black $Hole_{Index} = i$
10:	for $j$in$[1,···,M]$do
11:	$r_1 = rand()$
12:	if $r_1 \leq N_I(U_i)$ then
13:	White Hole $_{Index} = $ Roulette Wheel $_{Selection}(-N_I)$
14:	U(Black Hole$_{Index}$,j) $= S_U$(White Hole$_{Index}$,j)
15:	*end if*
16:	$r_2 = rand([0,I])$
17:	if $r_2 \leq W_{EP}$ then
18:	$r_3 = rand(), r_4 = rand()$
19:	if $r_3 < 0.5$ then
20:	$\omega_1 = ((ub(j) - lb(j)) \times r_4 + lb(j))$
21:	$U(i,j) = Best_u(j) + T_{DR} \times \omega$
22:	*else*
23:	$U(i,j) = Best_u(j) - T_{DR} \times \omega$
24:	*end if*
25:	*end if*
26:	*end for*
27:	*end for*
28:	$T_{HD} = Eval([U_1, U_2, ···, U_{Np}])$
29:	$Best_{THD_{ir}} = Max(T_{HD})$
30:	Δ Best $_{THD} = \frac{\sum_{k=1}^{M}\left(\text{Best } _{THD_k} - \text{ Best } _{THD_{k-1}} \right)}{M}$
31:	if Δ Best $_{THD<Tr}$ then ▷Perform hill climbing local search
32:	Best $_{THD} = $ Hill $-$clim$bing$ ($Best$ $_{THD}$)
33:	*end if*
34:	*end for*
35:	return U, Best $_{THD}$▷Final configuration
36:	**end procedure**

$$\Delta \text{ Best } _{THD} = \frac{\sum_{k=1}^{M}\left(\text{ Best } _{THD_k} - \text{ Best } _{THD_{k-1}} \right)}{M} \qquad (20)$$

where *BestTHDis* the best-found solution per generation, *andM* is related to the domain of iterations to compute the average performance of MVO. If the proposed best solution by the local search is better than the initial one, the global best of MVO will be updated. HCMVO iteratively runs hill climbing when the performance of MVO goes down, each time with an initial condition to prepare for escaping such undesirable situations. In order to get a better balance between exploration and exploitation, the search step size linearly decreases as follows:

$$S_t = S_t - \left(\frac{iter}{Max_{iter}} S_t \right) + 1 \qquad (21)$$

where *iter* and *Maxiter* are the current iteration and maximum number of evaluation, respectively. S_t stands for the step size of the neighborhood search. Meanwhile, this strategy can improve the convergence rate of MVO compared with other algorithms.

Algorithm 1 shows the technical details of the proposed optimization method (HCMVO). The initial solution includes freeboard (F), bottom elevation (B), number of ribs (Nr), rib thickness (R), and rib *height*(H).

5. Conclusion

The high trend of diminishing worldwide energy resources has entailed a great crisis upon vulnerable societies. To withstand this effect,

developing renewable energy technologies can open doors to a more reliable means, among which the wave energy converters will help the coastal residents and infrastructure. This paper set out to determine the optimized design for such devices that leads to the highest possible power output. The main goal of this research was to demonstrate the best design for an oscillating surge wave energy converter using a novel metaheuristic optimization algorithm. In this regard, the methodology was devised such that it argued the effects of influential parameters, including wave characteristics, WEC design, and interaction criteria.

To begin with, a numerical model was developed in Flow 3D software to simulate the response of the flap of a wave energy converter to incoming waves, followed by a validation study based upon a well-reputed experimental study to verify the accuracy of the model. Secondly, the hydrodynamics of the flap was investigated by incorporating the turbulence. The effect of depth, wave height, and wave period are also investigated in this part. The influence of two novel ideas on increasing the wave-converter interaction was then assessed: i) designing a flap with different widths in the upper and lower part, and ii) adding ribs on the surface of the flap. Finally, four trending single-objective metaheuristic optimization methods.

The implementation details of the hill-climbing algorithm applied in HCMPA can be seen in Algorithm 2. One of the critical parameters *isg*, which denotes the resolution of the neighborhood search around the proposed global best by MVO. If we set a small step size for hill-climbing, the convergence speed will be decreased. On the other hand, a large step size reinforces the exploration ability. Still, it may reduce the exploitation ability and in return increase the act of jumping from a global optimum or surfaces with high-potential solutions. Per each decision variable, the neighborhood search evaluates two different direct searches, incremental or decremental. After assessing the generated solutions, the best candidate will be selected to iterate the search algorithm. It is noted that the hill-climbing algorithm should not be applied in the initial iteration of the optimization process due to the immense tendency for converging to local optima. Meanwhile, for optimizing largescale problems, hill-climbing is not an appropriate selection. In order to improve understanding of the proposed hybrid optimization algorithm's steps, the flowchart of HCMVO is designed and can be seen in Fig. 16.

Fig. 17 shows the observed capture factor (which is the absorbed energy with respect to the available energy) by each optimization algorithm from iterations 1 to 400. The algorithms use ten search agents in their modified codes to find the optimal solutions. While GWO and MFO remain roughly constant after iterations 54 and 40, the other three algorithms keep improving the capture factor. In this case, HCMVO and MVO worked very well in the optimizing process with a capture factor obtained by the former as 0.594 and by the latter as 0.593. MFO almost found its highest value before the iteration 50, which means the exploration part of the algorithm works out well. Similarly, HCMVO does the same. However, it keeps finding the better solution during the optimization process until the last iteration, indicating the strong exploitation part of the algorithm. GWO reveals a weakness in exploration and exploitation because not only does it evoke the least capture factor value, but also the curve remains almost unchanged throughout 350 iterations.

Fig. 18 illustrates complex interactions between the five optimization parameters and the capture factor for HCMVO (a), MPA (b), and MFO (c) algorithms. The first interesting observation is that there is a high level of nonlinear relationships among the setting parameters that can make a multi-modal search space. The dark blue lines represent the best-found configuration throughout the optimisation process. Based on both HCMVO (a) and MVO (b), we can infer that the dark blue lines concentrate in a specific range, showing the high convergence ability of both HCMVO and MVO. However, MFO (c) could not find the exact optimal range of the decision variables, and the best-found solutions per
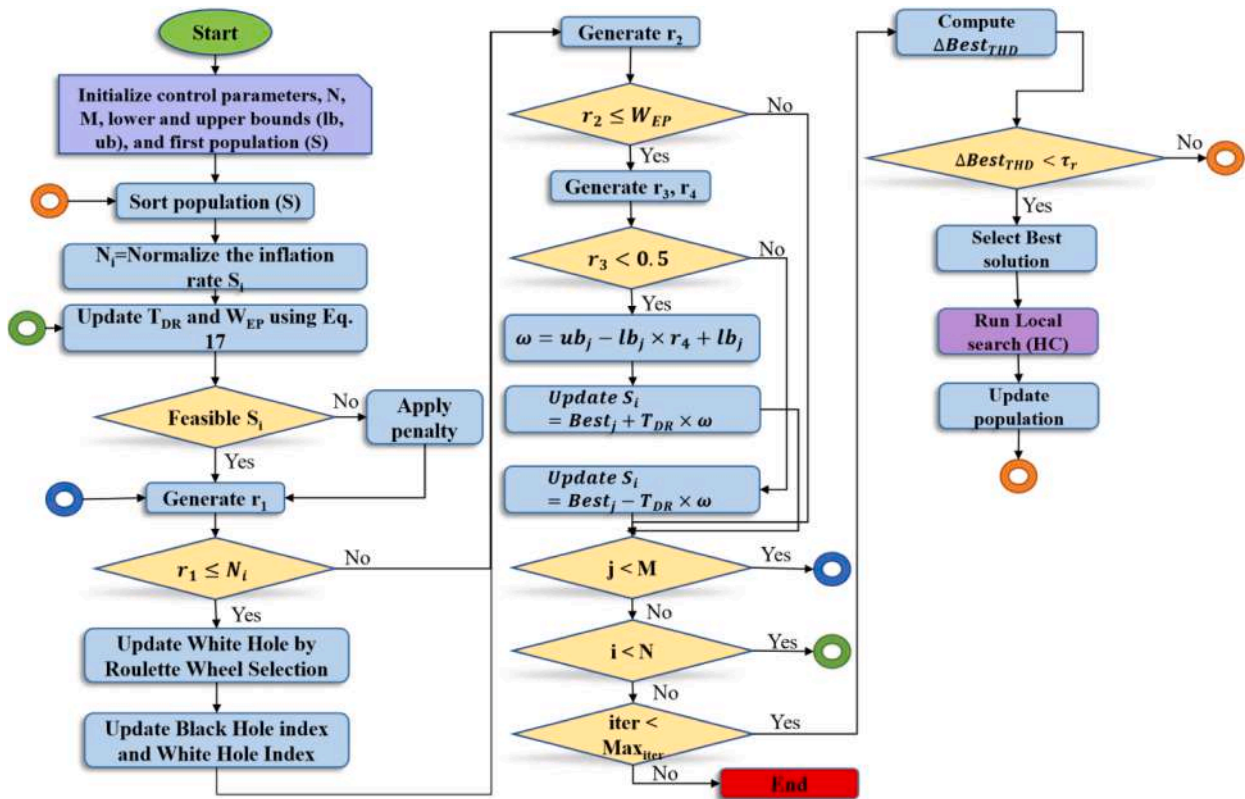
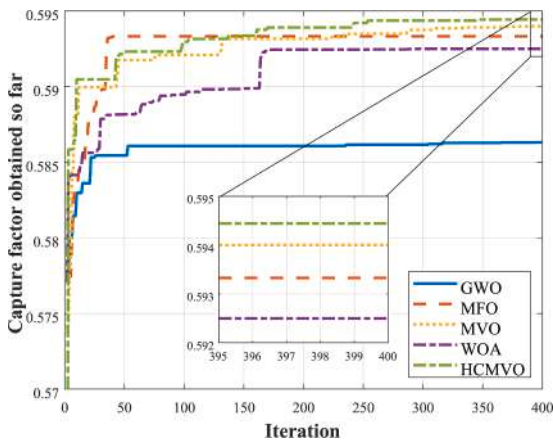**Fig. 16.** The flowchart of HCMVO Bi-level approach.

Fig. 17. Convergence curve for GWO, MFO, MVO, WOA, HCMVO optimization methods over the course of capture factor.

generation distribute mostly all around the search space.

	Algorithm 2: *Hill Climb Multiverse Optimization*
01:	procedure HCMVO
02:	**Initialization**
03:	Initialize the constraints lb_1^d, ub_1^d
04:	$S_1^d = \left(Min_1^d + Max_1^d\right)/g \triangleright$ Compute the step size, g is search resolution
05:	$Sol_1 = \{\langle F, B, N, R, H \rangle\} \triangleright$ *Initial solution*
06:	$(fitness_1) = Eval(Sol_1) \triangleright$ *Evaluate the solution*
07:	Main loop
08:	for iter $\leq Max_{ita=}$ do
09:	$Te_t = Te_t \pm S_t$
10:	while $t \leq len(Sol_1)$ do
11:	$Te_t = Te_t + S, \triangleright$ *Neighborhood search*
12:	$(fitness\ t_t^{iter}) = Eval(Te_t)$

(continued on next column)

(continued)

	Algorithm 2: *Hill Climb Multiverse Optimization*
13:	$t = t + 1$
14:	**end while**
15:	$\langle Max_{f_i}, Index\ x_{max} \rangle = Max(fitness)$
16:	$Sol_{itev} =$
	$Te_t(Index_{max}) \triangleright$ *Select the best feasible solution and update the design*
17:	$S_t = S_t - \left(\dfrac{iter}{Max}S_t\right) + 1 \triangleright S_t$ *linearly reduced*
18:	**end for**
19:	return Sol_{iter}, Max_f
20:	**end procedure**

were utilized to illuminate the optimum values of the design parameters, and the best method was chosen to develop a new algorithm that performs both local and global search methods.

The correlation between hydrodynamic parameters and the capture factor of the converter was supported by the results. For any given water depth, the capture factor increases as the wave period increases, until a certain wave period value (6 s) is reached, after which the capture factor gradually decreases. It is expected since the flap cannot oscillate effectively when the wavelength is too short for a certain water depth. Conversely, when the wavelength is too long, the capture factor decreases. Furthermore, under a constant wave period, increasing the water depth does not affect the capture factor. Regarding the sensitivity analysis, the study found that increasing the flap bottom elevation causes turbulence flow behind the flap and limitation of rotation, which leads to less interaction with the incoming waves. Furthermore, while keeping the flap bottom elevation constant, increasing the freeboard improves the capture factor. Overtopping happens when the freeboard is negative and the flap is below the water surface, which has a detrimental influence on converter performance. Furthermore, raising the freeboard causes the wave impact to become more violent, which increases converter performance.
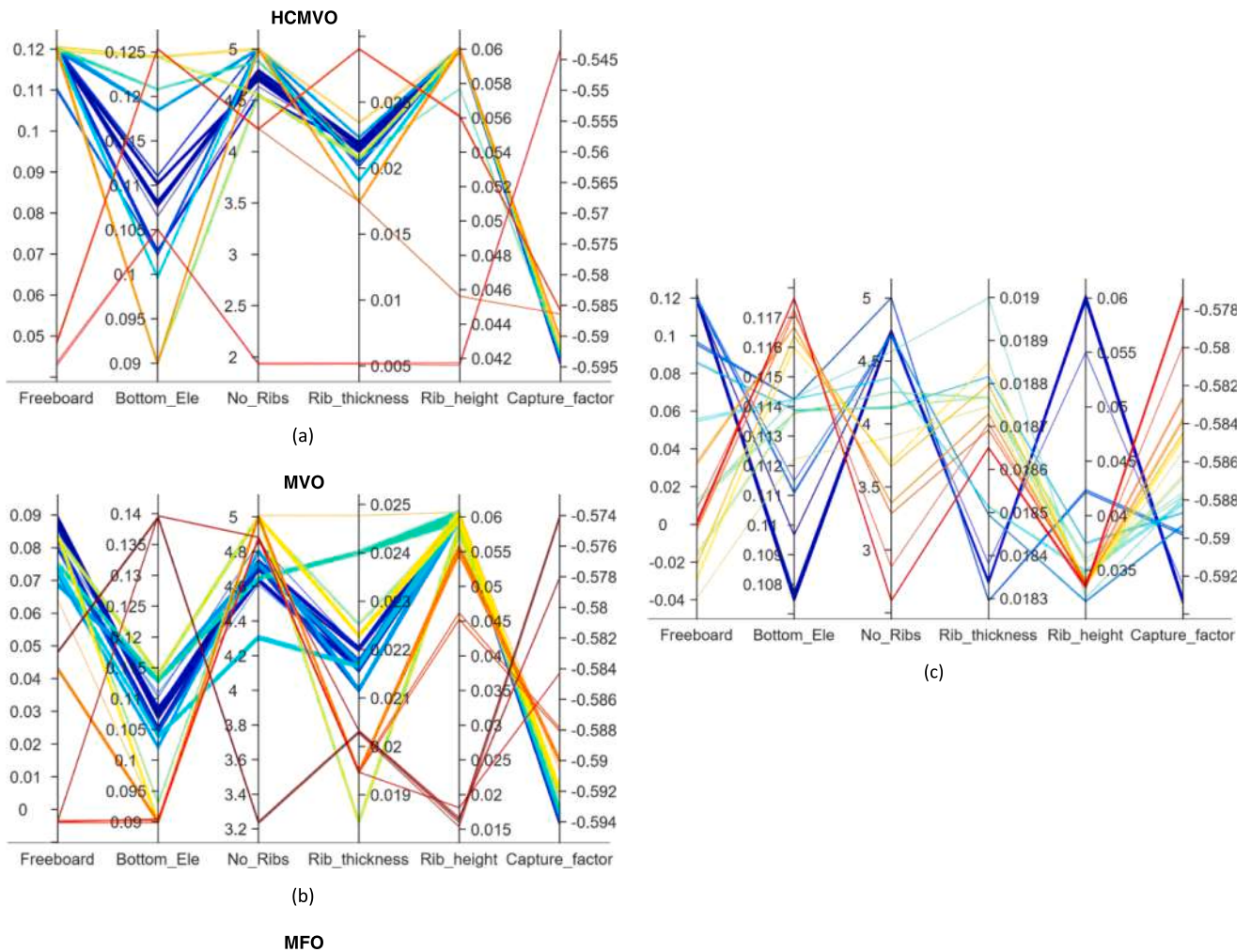
Fig. 18. Parallel visualization of best-performed optimization experiment for HCMVO, MVO and MFO. The dark blue lines show the best configuration of the five decision variables to achieve the highest rate of capture factor. (For interpretation of the references to color in this figure legend, the reader is referred to the web version of this article.)

In the last part, we discussed the search process of each algorithm and visualized their performance and convergence curves as they try to find the best values for decision variables. Among the four selected metaheuristic algorithms, the Multi-verse Optimizer proved to be the most effective in achieving the best answer in terms of the WEC capture factor. However, the MVO needed modifications regarding its escape approach from the local optima in order to improve its global search capabilities. To overcome these constraints, we presented a fast and efficient *meta*-algorithm (HCMVO) that combines MVO with a Random-restart hill-climbing local search. On a higher level, this *meta*-algorithm employed MVO to generate global tracking and present a range of possible and appropriate solutions. Taken together, the results demonstrated that there is a significant degree of nonlinearity among the setup parameters that might result in a multimodal search space. Since MVO was faced with a stagnation issue or fell into a local optimum, we constructed a complete neighborhood search around the best-found solution offered by the upper level. In sum, the newly-developed algorithm proved to be highly effective for the problem compared to other similar optimization methods. The strength of the current findings may encourage future investigation on design optimization of wave energy converters using developed geometry as well as the novel approach.

CRediT authorship contribution statement

Erfan Amini: Conceptualization, Methodology, Validation, Data

curation, Writing – original draft, Writing – review & editing, Visualization. **Mahdieh Nasiri:** Conceptualization, Methodology, Validation, Data curation, Writing – original draft, Writing – review & editing, Visualization. **Navid Salami Pargoo:** Writing – original draft, Writing – review & editing. **Zahra Mozhgani:** Conceptualization, Methodology. **Danial Golbaz:** Writing – original draft. **Mehrdad Baniesmaeil:** Writing – original draft. **Meysam Majidi Nezhad:** . **Mehdi Neshat:** Supervision, Conceptualization, Writing – original draft, Writing – review & editing, Visualization. **Davide Astiaso Garcia:** Supervision. **Georgios Sylaios:** Supervision.

Declaration of Competing Interest

The authors declare that they have no known competing financial interests or personal relationships that could have appeared to influence the work reported in this paper.

Data availability

Data will be made available on request.

Acknowledgement

References

[1] Ahmadpoor F, Sharma P. A perspective on the statistical mechanics of 2d materials. Extreme Mech Lett 2017;14:38–43.

[2] Azita Morteza, Masod Sadipour, Reza Saadati Fard, Saman Taheri, and Amirhossein Ahmadi. A dagging-based deep learning framework for transmission line flexibility assessment. *IET Renewable Power Generation*, 2022.

[3] Morteza A, Ilbeigi M, Schwed J. A blockchain information management framework for construction safety. Comput-ing Civ Eng 2021 2022.

[4] Jochem Weber, Ronan Costello, and John Ringwood. Wec technology performance levels (tpls)-metric for successful development of economic wec technology. *Proceedings EWTEC 2013*, 2013.

[5] Rahgooy K, Bahmanpour A, Derakhshandi M, Bagherzadeh-Khalkhali Aa. Distribution of elastoplastic modulus of subgrade reaction for analysis of raft foundations. Geomech Eng 2022;28(1):89–105.

[6] Eugen Rusuand Flor in Onea. Estimation of the wave energy conversion efficiency in the atlantic ocean close to the European islands. *Renewable Energy*, 85:687–703, 2016.

[7] Penalba M, Giorgi G, Ringwood JV. Mathematical modelling of wave energy converters: A review of nonlinear approaches. Renew Sustain Energy Rev 2017;78: 1188–207.

[8] Windt C, Davidson J, Ringwood JV. High-fidelity numerical modelling of ocean wave energy systems: A review of computational fluid dynamics-based numerical wave tanks. Renew Sustain Energy Rev 2018;93:610–30.

[9] Sheng W. Wave energy conversion and hydrodynamics modelling technologies: A review. Renew Sustain Energy Rev 2019;109:482–98.

[10] Ringwood JV, Bacelli G, Fusco F. Energymaximizing control of wave-energy converters: The development of control system technology to optimize their operation. IEEE Control Syst Mag 2014;34(5):30–55.

[11] Faedo N, Olaya S, Ringwood JV. Optimal control, mpc and mpc-like algorithms for wave energy systems: An overview. IFAC J Syst Control 2017;1:37–56.

[12] Wang L, Isberg J, Tedeschi E. Review of control strategies for wave energy conversion systems and their validation: the wave-to-wire approach. Renew Sustain Energy Rev 2018;81:366–79.

[13] Ringwood JV. Wave energy control: status and perspectives 2020. IFAC-PapersOnLine 2020;53(2):12271–82.

[14] Guo B, Ringwood JV. Geometric optimisation of wave energy conversion devices: A survey. Appl Energy 2021;297:117100.

[15] Amini E, Golbaz D, Asadi R, Nasiri M, Ceylan O, Nezhad MM, et al. A comparative study of metaheuristic algorithms for wave energy converter power take-off optimisation: A case study for eastern Australia. J Mar Sci Eng 2021;9(5):490.

[16] Pecher Arthur, Kofoed Jens Peter. Handbook of ocean wave energy. Springer Nature; 2017.

[17] Chang G, Jones CA, Roberts JD, Neary VS. A comprehensive evaluation of factors affecting the levelized cost of wave energy conversion projects. Renew Energy 2018;127:344–54.

[18] Amini E, Mehdipour H, Faraggiana E, Golbaz D, Mozaffari S, Bracco G, et al. Optimization of hydraulic power take-off system settings for point absorber wave energy converter. Renew Energy 2022;194:938–54.

[19] Garcia-Teruel A, Forehand DIM. A review of geometry optimisa-tion of wave energy converters. Renew Sustain Energy Rev 2021;139:110593.

[20] Nezhad MM, Heydari A, Neshat M, Keynia F, Piras G, Garcia DA. A mediterranean sea offshore wind classification using merra-2 and machine learning models. Renew Energy 2022;190:156–66.

[21] López I, Andreu J, Ceballos S, Alegría IMD, Kortabarria I. Review of wave energy technologies and the necessary power-equipment. Renew Sustain Energy Rev 2013;27:413–34.

[22] Ekström R, Ekergård B, Leijon M. Electrical damping of linear generators for wave energy converters—a review. Renew Sustain Energy Rev 2015;42:116–28.

[23] Danial Golbaz, Rojin Asadi, Erfan Amini, Hossein Mehdipour, Mahdieh Nasiri, Meysam Majidi Nezhad, Seyed Taghi Omid Naeeni, and Mehdi Neshat. Ocean wave energy converters optimization: A comprehensive review on research directions. *arXiv preprint arXiv:2105.07180*, 2021.

[24] Michael Choiniere, Jacob Davis, Nhu Nguyen, Nathan Tom, Matthew Fowler, and Krish Thiagarajan Sharman. Hydrodynamics and load shedding behavior of a variable geometry oscillating surge wave energy converter (oswec). *Available at SSRN 3900951*, 2022.

[25] Alan Henry, Olivier Kimmoun, Jonathan Nicholson, Guillaume Dupont, Yanji Wei, andFrederic Dias. A two dimensional experimental investigation of slamming of an oscillating wave surge converter. In *The Twenty-fourth International Ocean and Polar Engineering Conference*. OnePetro, 2014.

[26] Doyle S, Aggidis GA. Development of multioscillating water columns as wave energy converters. Renew Sustain Energy Rev 2019;107:75–86.

[27] Doyle S, Aggidis GA. Experimental investigation and performance comparison of a 1 single owc, array and m-owc. Renew Energy 2021;168:365–74.

[28] Matthew Folley, T.J.T. Whittaker, Alan Henry, The effect of water depth on the performance of a small surging wave energy converter. *Ocean Eng*, 34(8-9): 1265–1274, 2007.

[29] Li Q, Mi J, Li X, Chen S, Jiang B, Zuo L. A self-floating oscillating surge wave energy converter. Energy 2021;230:120668.

[30] Sarkar D, Renzi E, Dias F. Effect of a straight coast on the hydrodynamics and performance of the oscillating wave surge converter. Ocean Eng 2015;105:25–32.

[31] Adrian de Andres, Jéromine Maillet, Jørgen Hals Todalshaug, Patrik Möller, and Henry Jeffrey. On the optimum sizing of a real wec from a techno-economic perspective. In *International Conference on Offshore Mechanics and Arctic Engineering*, volume 49972, page V006T09A013. American Society of Mechanical Engineers, 2016.

[32] Schmitt P, Elsaesser B. On the use of openfoam to model oscillating wave surge converters. Ocean Eng 2015;108:98–104.

[33] Wang D-J, Qiu S-Q, Ye J-W. Width effects on hydrodynamics of pendulum wave energy converter. Appl Math Mech 2014;35(9):1167–76.

[34] Whittaker T, Folley M. Nearshore oscillating wave surge converters and the development of oyster. Philos Trans Sci R Soc A: Math, Phys Eng 2012;370(1959): 345–64.

[35] Louise O'Boyle, Kenneth Doherty, Jos van't Hoff, and Jessica Skelton. The value of full scale prototype data-testing oyster 800 at emec, orkney. In *Proceedings of the 11th European wave and tidal energy conference (EWTEC), Nantes, France*, pages 6–11, 2015.

[36] Why flow-3d? https://www.flow3d.com/products/flow-3d/ why-flow-3d/, 2022.

[37] Ishmail B Celik, Urmila Ghia, Patrick J Roache, and Christopher J Freitas. Procedure for estimation and reporting of uncertainty due to discretization in cfd applications. *Journal of fluids EngineeringTransactions of the ASME*, 130(7), 2008.

[38] Pal Schmitt, K Doherty, Darragh Clabby, and T Whittaker. The opportunities and limitations of using cfd in the development of wave energy converters. *Marine & Offshore Renewable Energy*, pages 89–97, 2012.

[39] Choiniere M, Davis J, Nguyen Nu, Tom N, Fowler M, Thiagarajan K. Hydrodynamics and load shedding behavior of a variable-geometry oscillating surge wave energy converter (oswec). Renew Energy 2022.

[40] Yong Li and Mian Lin. Regular and irregular wave impacts on floating body. *Ocean Engineering*, 42:93–101, 2012. Pal Manuel Schmitt. *Investigation of the near flow field of bottom hinged flap type wave energy converters*. PhD thesis, Queen's University Belfast, 2014.

[41] Alan John Henry. *The hydrodynamics of small seabed mounted bottom hinged wave energy conerverters in shallow water*. PhD thesis, Queen's University Belfast, 2009.

[42] Ghorbani N, Korzeniowski A, et al. Adaptive risk hedging for call options under cox-ingersoll-ross interest rates. J Math Finance 2020;10(04):697.

[43] Renzi E, Dias F. Relations for a periodic array of flap-type wave energy converters. Appl Ocean Res 2013;39:31–9.

[44] Abdel-Basset M, Abdel-Fatah L, Sangaiah AK. Chapter 10metaheuristic algorithms: a comprehensive review. Computational intelligence for multimedia big data on the cloud with engineering applications. 2018.

[45] Mirjalili S, Mirjalili SM, Lewis A. Grey wolf optimizer. Adv Eng Softw 2014;69: 46–61.

[46] Mirjalili S. Moth-flame optimization algorithm: A novel natureinspired heuristic paradigm. Knowl-Based Syst 2015;89:228–49.

[47] Mohammad Shehab, Laith Abualigah, Husam Al Hamad, Hamzeh Alabool, Mohammad Alshinwan, and Ahmad M Khasawneh. Moth– flame optimization algorithm: variants and applications. *Neural Comput Appl*, 32(14):9859–9884, 2020.

[48] Yıldız Betül Sultan, Yıldız Ali Rıza. Moth-flame optimization algorithm to determine optimal machining parameters in manufacturing processes. Materials Testing 2017;59(5):425–9.

[49] M Tegmark. Barrow, jd davies, pc harper, cl, jr eds. *Science and Ultimate Reality Cambridge University Press Cambridge*, 2004.

[50] Douglas MEardley. Death of white holes in the early universe. *Phys Rev Lett*, 33(7): 442, 1974.

[51] Davies PCW. Thermodynamics of black holes. Reports on Progress in Physics 1978; 41(8):1313.

[52] Morris MS, Thorne KS. Wormholes in spacetime and their use for interstellar travel: A tool for teaching general relativity. Am J Phys 1988;56(5):395–412.

[53] Mirjalili S, Mirjalili SM, Hatamlou A. Multi-verse optimizer: a nature-inspired algorithm for global optimization. Neural Comput & Appl 2016;27(2):495–513.

[54] Mirjalili S, Lewis A. The whale optimizationalgorithm. Adv Eng Softw 2016;95: 51–67.

[55] Gharehchopogh Farhad Soleimanian, Gholizadeh Hojjat. A comprehensive survey: Whale optimization algorithm and its applications. Swarm Evol Comput 2019;48: 1–24.

[56] Abualigah L. Multi-verse optimizer algorithm: a comprehensive survey of its results, variants, and applications. Neural Comput Appl 2020;32(16):12381–401.